energies

MDPI

Article

Impedance Reshaping Strategy for Battery Energy Storage Systems Based on Partial Power Conversion

Ming Li [1], Yucheng Wu [1,*], Xiangxin Xi [1], Haibo Liu [1], Baizheng Xu [2,*] and Long Jing [3]

[1] Aerospace Changfeng Chaoyang Power Co., Ltd., Beijing Aerospace Changfeng Co., Ltd., Beijing 122001, China; funkeycard@163.com (M.L.); cydyxxx@163.com (X.X.); cydylhb@163.com (H.L.)
[2] Dongying Power Supply Company, State Grid Shandong Electric Power Company, Dongying 257000, China
[3] National Energy Active Distribution Network Technology R&D Center, Beijing Jiaotong University, Beijing 100044, China; ljing@bjtu.edu.cn
* Correspondence: 21121515@bjtu.edu.cn (Y.W.); 15611231192@163.com (B.X.)

Abstract: To avoid additional component losses while significantly improving the energy conversion efficiency of battery energy storage systems, the application of series-connected partial power converter (S-PPC) technology in battery energy storage systems is investigated in this study. In the S-PPC battery energy storage system configuration, coupling effects exist between the dc-link side and the battery-series side. The impedance modeling of a battery energy storage system is performed while taking these coupling effects into consideration. To address the instability observed during battery discharge conditions, an impedance reshaping control strategy that is suitable for the S-PPC battery energy storage system is proposed. The proposed method focuses on adjusting the input impedance of the load converter within a limited frequency band centered on the system's oscillation frequency. This targeted approach significantly improves the stability of the system while ensuring ease of implementation and maintaining high reliability. Finally, the experimental results validate the theoretical analysis.

Keywords: partial power conversion; battery energy storage system; impedance modeling; stability analysis; impedance reshaping

check for updates

Received: 29 November 2024
Revised: 27 December 2024
Accepted: 3 January 2025
Published: 4 January 2025

Citation: Li, M.; Wu, Y.; Xi, X.; Liu, H.; Xu, B.; Jing, L. Impedance Reshaping Strategy for Battery Energy Storage Systems Based on Partial Power Conversion. *Energies* **2025**, *18*, 189. https://doi.org/10.3390/en18010189

Copyright: © 2025 by the authors. Licensee MDPI, Basel, Switzerland. This article is an open access article distributed under the terms and conditions of the Creative Commons Attribution (CC BY) license (https://creativecommons.org/licenses/by/4.0/).

1. Introduction

To reduce the effects of integrating large-scale renewable energy into the grid, battery storage systems are installed near these energy sources to ensure a stable power supply [1–3]. During the construction of a battery energy storage system, to meet the high-voltage and large-capacity demands of the system, it is necessary to connect numerous battery cells in series and in parallel, which are then linked to high-voltage conversion equipment. However, differences in parameters such as capacity and internal resistance among individual cells can lead to inconsistencies in the overall capacity of the battery pack, thereby affecting the effective capacity and operational efficiency of the entire energy storage system [4–6].

To address the inconsistencies in battery packs, DC/DC converters can be employed to balance the cells within groups, maximizing battery utilization and enhancing the efficiency and reliability of energy storage systems [7–9]. However, as the power demands of these systems continue to grow, traditional full-power processing (FPP) schemes encounter limitations in terms of efficiency, cost, and thermal management. To resolve these issues, some researchers have proposed the partial power converter (PPC) scheme, in which power flow between the source and the load is controlled such that most of the power is

transmitted directly between them, and the DC/DC converter only handles a small portion of the power. This reduces the rated power of the DC/DC converter, thus minimizing additional component losses [10,11].

The PPC scheme consists of parallel current regulation and series voltage regulation, which are realized using parallel-connected partial power converters (P-PPCs) and series-connected partial power converters (S-PPCs), respectively [12]. The P-PPC primarily addresses power issues arising from current mismatches between adjacent sources or components. Its limitation lies in the fact that the number of required DC/DC converters is proportional to the number of system components, which significantly increases costs in large-scale power applications. The P-PPC is widely used in applications such as those that regulate current differences between photovoltaic arrays and coordinate output power differences between wind turbines [13–15].

The S-PPC has the capability to perform voltage conversion and power flow control between the source and the load. It is limited to handling the power flow caused by voltage differences between the source and load terminals. Depending on whether the two sides of the DC/DC converter share a common ground, it can be further classified into non-co-ground (nCG) and co-ground (CG) topologies [16], as shown in Figure 1. The nCG-type S-PPC must use an isolated DC/DC converter topology, which reduces the cost and volume while improving power density and thermal management. However, when facing sudden voltage changes on the dc-link side, the instantaneous source–load voltage difference directly clamps the DC/DC converter port, causing the processed power to exceed the rated value of the internal DC/DC converter. Additionally, when the voltage adjustment ratio is too large, the system efficiency becomes relatively low [17–19]. The CG-type S-PPC allows for either isolated or non-isolated DC/DC converter topologies and is mostly applied in battery energy storage systems that do not require grounding [20–23].

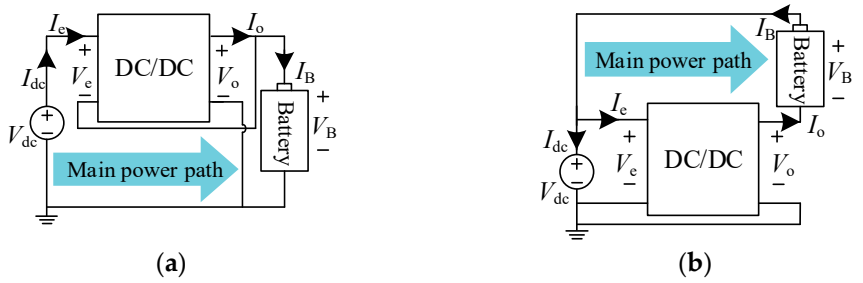


Figure 1. S-PPC structure topology: (**a**) non-co-grounded S-PPC structure; (**b**) co-grounded S-PPC structure.

By comparison, S-PPCs generally exhibit a superior suitability for battery energy storage systems compared to P-PPCs. By directly regulating the bus voltage and processing only the voltage difference between the battery stack and the bus, S-PPCs accommodate the wide voltage range of batteries while substantially simplifying the control architecture and improving overall efficiency. In contrast to P-PPCs, which primarily focus on current regulation, S-PPCs handle a significantly reduced portion of the total power, thereby lowering the power rating and thermal management requirements for semiconductor devices, as well as reducing overall system cost and size. Throughout the charging and discharging cycle, S-PPCs maintain stable and efficient control of the bus voltage; this makes them particularly advantageous for large-scale battery energy storage systems deployed in high-voltage DC bus or microgrid environments.

S-PPC systems offer potential cost advantages by reducing converter power ratings, lowering initial investment, and minimizing operational losses. Moreover, the reduced energy processing of S-PPC systems aligns with sustainability goals by decreasing greenhouse gas emissions and improving material efficiency.

When S-PPC technology is applied to complex systems, the interaction between input and output, as well as the coupling effects between the cascaded stages of the converters, can lead to a decline in overall system stability, potentially resulting in voltage and current oscillations in severe cases. Therefore, the impedance modeling of the S-PPC and stability analysis are particularly important. In [24], a general method that is suitable for PWM converters operating in continuous conduction mode (CCM) is proposed; it is used to solve dynamic equations and AC small-signal relationships for the input–output voltage and duty cycle–output voltage transfer functions in the PPC. However, this method is not applicable to resonant converters. The authors of [25,26] applied PPC technology to distributed photovoltaic systems, analyzing the control loop of maximum power point tracking (MPPT) but without constructing an impedance model. In [27], the authors analyzed the working principles and characteristics of the S-PPC, establishing a small-signal model for the converter. However, since the isolated DC/DC input and output were connected in series, it was assumed during analysis that input voltage disturbances were nonexistent, which prevented reflection on the influence of disturbances from the isolated DC/DC output on the input.

In response to the instability of the DC/DC cascaded system, the authors of [28] analyzed the impedance characteristics of the converter and the influencing factors of the corresponding parameters and proposed an optimization scheme to reduce the output impedance of the source converter. The authors of [29] proposed three passive damping optimization strategies aimed at reducing the resonant peaks of the source-side converter's output impedance and ensuring that the output impedance, Z_{oS}, of the source converter remained below the input impedance, Z_{iL}, of the load converter across the entire frequency range. However, these optimization measures may introduce additional energy losses, which could adversely affect the overall efficiency of the converter. In [30–32], an inductor current was introduced into the control loop, which modified the inductive damping of the source converter to reduce its output impedance. However, altering the output impedance of the source converter through active damping may lead to a deterioration in the system's dynamic performance.

In a battery energy storage system utilizing S-PPC technology, the coupling between the dc-link side and the battery-series side, as well as the interaction between the cascaded converter stages, can impact the stability of the entire energy storage system. Therefore, impedance modeling is conducted in this study with careful consideration of these coupling effects. Additionally, a damping reshaping method is proposed for the S-PPC battery energy storage system to enhance system stability.

The structure of this paper is as follows: Section 1 introduces the research and provides background information to the reader. Section 2 describes the structure of the CG-type S-PPC battery energy storage system and performs impedance modeling while considering coupling effects. Section 3 introduces a strategy for enhancing the stability of the battery energy storage system by adding a virtual impedance parallel to the load-side input impedance. This modification adjusts the interaction between the output impedance of the source converter and the input impedance of the load converter, thereby improving system stability. Section 4 demonstrates the effectiveness of the proposed approach through simulation and experimental validation. Finally, Section 5 provides a summary of the work presented in this paper.

2. Modeling of S-PPC Energy Storage System

2.1. Principle Analysis

The CG S-PPC battery energy storage converter, which is shown in Figure 2, is examined in this study. This converter consists of three parts: an LLC resonant circuit, an

H-bridge circuit, and a solid-state circuit breaker. The LLC resonant circuit operates in a fixed-frequency resonant state, with its input connected to the dc link or load and its output cascaded with the H-bridge circuit. The output of the H-bridge circuit is connected in series with the battery. The solid-state circuit breaker assists in the safe startup of the battery energy storage converter and protects the converter from significant voltage differentials in the event of a short-circuit fault [33]. The dc link is responsible for providing all the charging and discharging power, with the majority of the power being directly delivered to the battery through the dc link, while a small portion of the power is transmitted to the battery through the LLC resonant circuit and the H-bridge circuit.

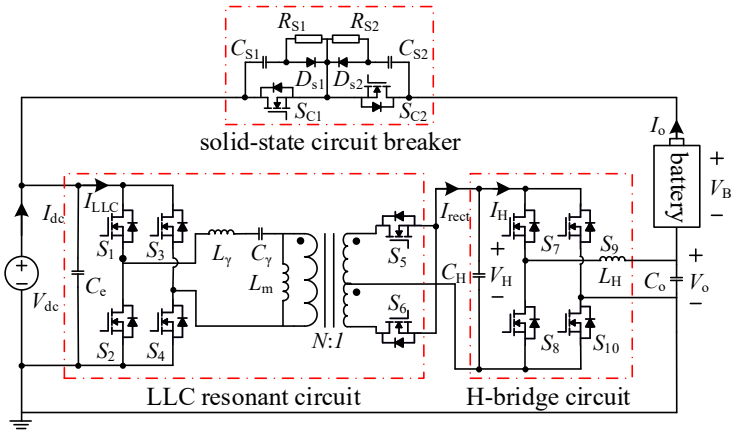


Figure 2. The configuration of the CG S-PPC battery energy storage converter, where V_{dc} denotes the dc-link voltage; I_{dc} is the dc-link current; I_{LLC} is the current flowing into the LLC resonant circuit; I_{rect} is the current input to the H-bridge circuit by the LLC resonant circuit; V_H is the output voltage of the H-bridge circuit; V_B is the battery voltage; and I_o represents the output current of the H-bridge circuit and the current flowing through the battery.

In Figure 2, the output voltage V_H of the H-bridge circuit is the difference between the dc-link voltage V_{dc} and the voltage across the battery terminals V_B. A voltage constraint relationship exists and is defined as follows:

$$V_{dc} = V_B + V_o \tag{1}$$

Under the same battery power conditions, the FPP converter is utilized to handle the entire battery power, whereas the PPC handles less power than the battery power, thus reducing system operating losses. Most of the energy is exchanged between the dc link and the battery. The ratio of the converter handling power to the battery power is denoted as K_{pr} and is defined as

$$K_{pr} = \frac{P_c}{P_B} \tag{2}$$

where P_c is the processing power of the converter, and P_B is the battery power.

The power loss P_{loss} flowing through the LLC resonant circuit and the H-bridge circuit is

$$P_{loss} = (1 - \eta_c) \cdot P_c \tag{3}$$

where η_c is the overall efficiency of the LLC resonant converter and the H-bridge circuit.

Under the condition of battery charging, the dc link is utilized as a source to deliver energy to the battery. At this time, the efficiency η_c of the S-PPC battery energy storage system is

$$\eta_c = \frac{P_B}{P_{loss} + P_B} = \frac{1}{P_{loss}/P_B + 1} \tag{4}$$

By combining (2), (3), and (4), the efficiency relationship of the S-PPC battery energy storage system under battery charging conditions is obtained as follows:

$$\eta_c = \frac{1}{P_{loss}/P_B + 1} = \frac{1}{K_{pr}(1-\eta_c)+1} = \eta_c + \frac{(1-\eta_c)(1-K_{pr}\eta_c)}{K_{pr}(1-\eta_c)+1} \tag{5}$$

Under battery discharge conditions, the battery is utilized as a source to deliver energy to the dc link, at which point the efficiency of the S-PPC battery energy storage system η_{disc} is given by

$$\eta_{disc} = \frac{P_B - P_{loss}}{P_B} = 1 - \frac{P_{loss}}{P_B} \tag{6}$$

The efficiency relationship of the S-PPC battery energy storage system under battery discharge conditions is obtained by combining (2), (3), and (6) and is expressed as follows:

$$\eta_{disc} = 1 - \frac{P_{loss}}{P_B} = 1 - K_{pr}(1-\eta_c) = \eta_c + (1-\eta_c)(1-K_{pr}) \tag{7}$$

It can be inferred from (2), (5), and (7) that the converter efficiency η_c is less than 1. When η_c remains constant, a smaller efficiency ratio K_{pr} results in a higher efficiency of the S-PPC battery energy storage system.

The CG S-PPC battery energy storage converter demonstrates significant potential to reduce overall system costs, which is a critical consideration for its large-scale deployment. By limiting the power processed by the converter, S-PPC technology reduces the size, cost, and thermal management requirements of key components, leading to lower capital investment. Additionally, the inherent efficiency improvements minimize operational energy losses, translating into long-term cost savings. These attributes position the CG S-PPC battery energy storage converter as a cost-effective alternative to traditional full-power processing systems, particularly for high-capacity battery energy storage applications.

2.2. System Modeling

The LLC resonant converter includes a switching frequency and its harmonic components, and its small-signal model is established using the extended describing function. In the literature [34], the LLC resonant converter is analyzed through the extended describing function, resulting in a simplified equivalent small-signal circuit model, which is shown in Figure 3.

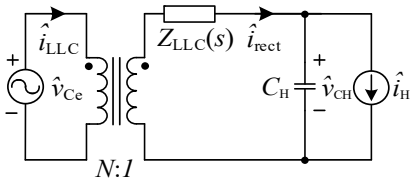


Figure 3. LLC resonant converter small-signal model.

The $Z_{LLC}(s)$ expression in Figure 3 is

$$Z_{LLC}(s) = sL_\gamma \frac{\pi^2}{4N^2} \tag{8}$$

From the small-signal model in Figure 3, the input impedance $Z_{i_LLC}(s)$ of the LLC resonant converter and the output impedance $Z_{o_LLC}(s)$ are derived:

$$\begin{aligned} Z_{i_LLC}(s) &= \frac{N^2((sCR+1)Z_{LLC}(s)+R)}{sCR+1} \\ Z_{o_LLC}(s) &= \frac{Z_{LLC}(s)}{sCZ_{LLC}(s)+1} \end{aligned} \tag{9}$$

where R is the load impedance of the LLC resonant converter.

The control block diagram of the H-bridge is shown in Figure 4. In the diagram, $\hat{v}_H$ represents the small-signal disturbance of the H-bridge input voltage, $\hat{i}_H$ represents the small-signal disturbance of the H-bridge input current, $\hat{v}_o$ represents the small-signal disturbance of the H-bridge output voltage, io represents the small-signal disturbance of the H-bridge output current, and $\hat{d}$ represents the small-signal disturbance of the H-bridge duty cycle. $G_v(s)$ denotes the voltage loop PI regulator, $G_i(s)$ denotes the current loop PI regulator, and H_i and H_v represent the sampling coefficients of the H-bridge inductance current and output voltage, respectively. The transfer function of the H-bridge is shown in Table 1.

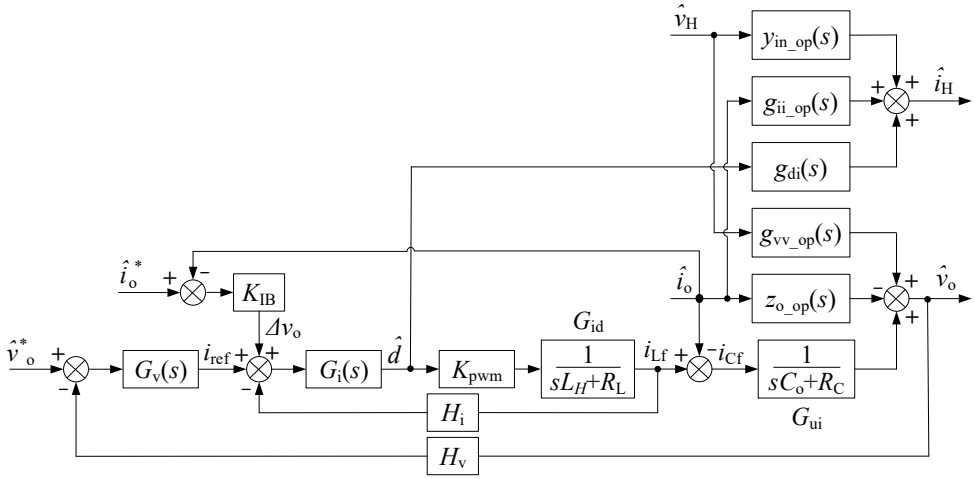


Figure 4. Control block diagram of H-bridge circuit.

Table 1. Expressions of transfer functions of H-bridge.

Symbol	Symbolic Meaning	Formula
$y_{in_op}(s)$	Input admittance	D^2C_os/G_1
$g_{ii_op}(s)$	Load-to-input current transfer function	$D(R_cC_os+1)/G_1$
$g_{di}(s)$	Control-to-input current transfer function	$P/V_o + V_oC_os/G_1$
$g_{vv_op}(s)$	Input-to-output voltage transfer function	$D(R_cC_os+1)/G_1$
$z_{o_op}(s)$	Output impedance	$-(sL_H + R_L)(R_cC_os+1)/G_1$

In Table 1, D, V_H, and V_o denote the steady-state values of d, v_H, and v_o, respectively. The transfer function $G_1(s)$ can be expressed as

$$G_1(s) = L_HC_os^2 + (R_LC_o + R_CC_o)s + 1 \tag{10}$$

The open-loop gain $G_{op}(s)$ of the H-bridge is expressed as

$$G_{op}(s) = \frac{G_v(s) \cdot G_i(s) \cdot K_{PWM} \cdot G_{id} \cdot G_{vi} \cdot H_v}{1 + G_i(s) \cdot K_{PWM} \cdot G_{id} \cdot H_i} \tag{11}$$

In Figure 2, the output voltage V_o of the H-bridge circuit is coupled with the dc-link voltage V_{dc} through the series connection of the battery voltage V_B. The dc-link voltage serves as the input of the LLC resonant circuit. When there is a sudden change in the dc-link voltage command or load, the output voltage V_o is influenced by the direct disturbance of the output current I_o and the disturbance transmitted through the LLC resonant circuit, which can lead to stability issues in the S-PPC battery energy storage system. According to the influence on the input voltage V_{dc} of the LLC resonant circuit caused by the output

voltage V_o of the H-bridge circuit and the input current I_{LLC} of the LLC resonant circuit, as well as the influence on the output voltage V_o of the H-bridge circuit caused by the input voltage V_{dc} of the LLC resonant circuit and the output current I_o of the H-bridge circuit, the following equations can be derived:

$$\begin{bmatrix} \hat{v}_{dc} \\ \hat{v}_o \end{bmatrix} = \begin{bmatrix} Z_1 & 0 \\ 0 & Z_2 \end{bmatrix} \begin{bmatrix} \hat{i}_1 \\ \hat{i}_2 \end{bmatrix} + \begin{bmatrix} 0 & k_{12} \\ k_{21} & 0 \end{bmatrix} \begin{bmatrix} \hat{v}_o \\ \hat{v}_{dc} \end{bmatrix} \tag{12}$$

where Z_1 is the dc-link impedance; k_{12} is the transfer function of V_{dc} to V_o; Z_2 is the LLC output impedance; and k_{21} is the transfer function of V_o to V_{dc}.

Since $\hat{i}_{LLC} \approx \hat{i}_o$, the following can be derived:

$$\begin{aligned} Z_{s1} &= \frac{\hat{v}_{dc}}{\hat{i}_o} = \frac{Z_1 + k_{12}Z_2}{1 - k_{12}k_{21}} \\ Z_{s2} &= \frac{\hat{v}_o}{\hat{i}_o} = \frac{k_{21}Z_1 + Z_2}{1 - k_{12}k_{21}} \end{aligned} \tag{13}$$

Through the aforementioned derivation, the impedance model of the S-PPC battery energy storage system is obtained, as illustrated in Figure 5. The system is equivalently represented as two voltage sources in series with their internal resistances.

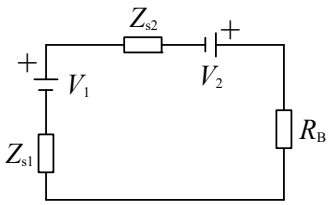


Figure 5. Impedance model of S-PPC battery energy storage system.

In Figure 5, Z_{s1} represents the impedance on the dc link, which is parallel with the input impedance of the LLC resonant circuit, and Z_{s2} represents the output impedance of the H-bridge circuit. Their expressions are as follows:

$$\begin{aligned} Z_{S1} &= Z_{dc}(s) \parallel Z_{LLC_i}(s) \\ Z_{S2} &= Z_{o_op}(s) \end{aligned} \tag{14}$$

k_{12} represents the product of the transfer function from v_{dc} to v_H in the LLC resonant circuit and the transfer function from v_H to the output voltage v_o in the H-bridge circuit. Similarly, k_{21} represents the product of the transfer function from v_o to v_{dc} in the LLC resonant circuit and the transfer function from v_o to v_H in the H-bridge circuit. Their expressions are as follows:

$$\begin{aligned} k_{12} &= A_{v_LLC_in/o}(s)/g_{vv_op}(s) \\ k_{21} &= g_{vv_op}(s)/A_{v_LLC_in/o}(s) \end{aligned} \tag{15}$$

The transfer function of the LLC resonant circuit from v_{dc} to v_H is represented through impedance voltage division:

$$A_{v_LLC_in/o} = \frac{NZ_{dc}(s)}{Z_{dc}(s) + Z_{LLC}(s)} \tag{16}$$

3. Stability Improvement Strategies for Battery Energy Storage Systems

3.1. Stability Analysis of Battery Energy Storage Systems

Through the modeling derivation process, it can be shown that the stability of the equivalent impedance model of the S-PPC battery energy storage system is affected not only by its own physical parameters but also by the control parameters in control loops such as the outer voltage loop and the inner current loop, as well as different operating conditions. Using the simplified equivalent impedance model, the system is analyzed in two scenarios involving the source and load converters. During battery charging, energy is supplied to the dc link, with V_1 and V_2 connected in series as the source converter and R_B functioning as the load converter. Conversely, during battery discharging, energy flows from the battery to the dc link, where V_2 and R_B constitute the load converter, and V_1 operates as the source converter. The stability analysis for the cascaded system remains consistent across both scenarios. If the stability criteria are satisfied under the worst-case conditions, the system can be deemed stable.

Energy is provided on the dc-link side in the battery charging condition, with V_1 and V_2 connected in series, forming the source converter, and R_B being the load converter. The Bode plot under this condition is shown in Figure 6. Under this condition, the load converter R_B can be approximated as a resistive load. Even when the converter system operates under harsh full-load conditions, the phase curve does not exceed 135°, although the magnitude curves intersect. Therefore, the provision of energy on the dc-link side for battery charging will not result in instability.

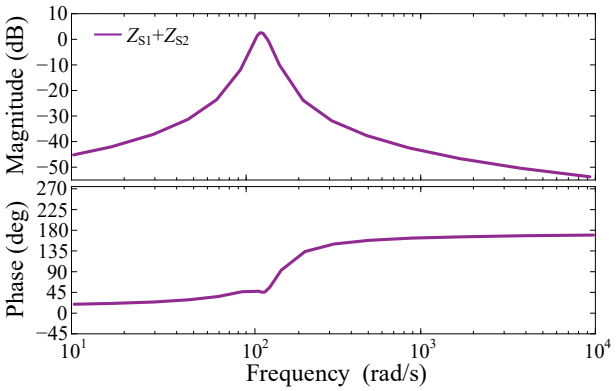


Figure 6. Bode plot for battery charging condition.

Figure 7 shows the Bode plots of the load converter $Z_{S2} + R_B$ and the source converter Z_{S1}, as well as the Nyquist plot of the impedance ratio $T_m = (Z_{S2} + R_B)/Z_{S1}$, with the dc link as the source and with the converter handling one-quarter of the battery discharge power. As shown in Figure 7a, the input voltage V_{dc} of the LLC converter influences the output voltage V_o of the H-bridge, leading to amplitude–frequency curve intersections at 650 Hz and 1000 Hz. Notably, only the phase difference at 1000 Hz exceeds 180°. This phenomenon causes the Nyquist plot of T_m in Figure 7b to encircle the critical point (−1, 0), with $|T_m| > 1$ signifying system instability under these conditions.

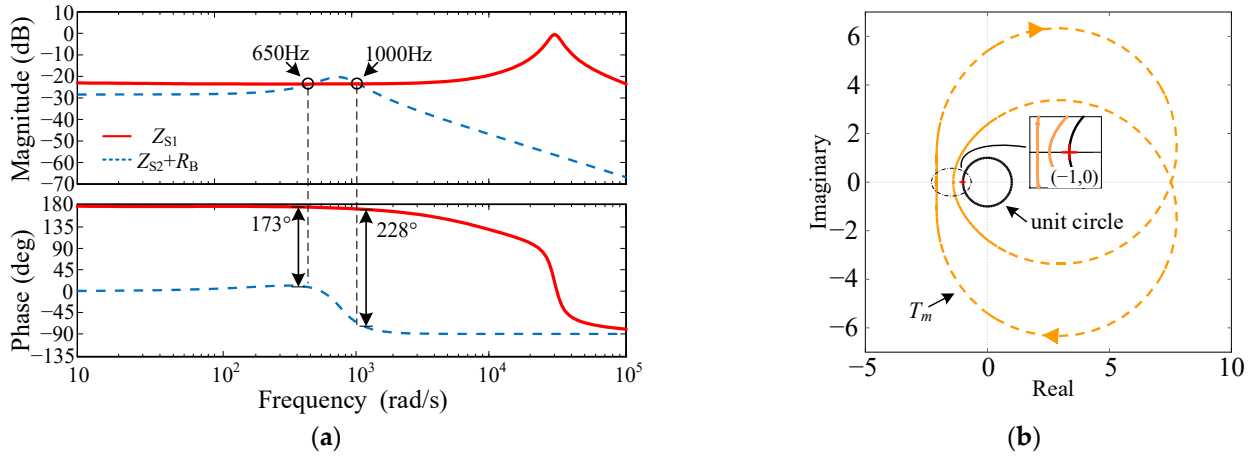


Figure 7. Bode and Nyquist plots for battery discharge conditions: (**a**) Bode plots of $Z_{s2} + R_B$ and Z_{s1}; (**b**) Nyquist plot of T_m.

3.2. Stability Improvement Mechanisms for Battery Energy Storage Systems

Figure 8 demonstrates a mechanism for enhancing system stability, where Z_{os} and Z_{il} represent the output impedance of the source converter and the input impedance of the load converter, respectively. For a switch-mode power supply used as the source converter, f_{cS} denotes the cutoff frequency of its voltage loop; for an LC filter, f_{cS} corresponds to the filter's resonant frequency. Similarly, f_{cL} refers to the cutoff frequency of the load converter's voltage loop, while Z_{oSP} is the peak value of Z_{oS}. System instability arises when Z_{oS} intersects with Z_{iL} and f_{cS} is lower than f_{cL}, causing the cascaded system to become unstable despite the individual stability of its subsystems. This instability is primarily driven by a $-180°$ phase shift, which results from the negative resistance characteristics of the load converter.

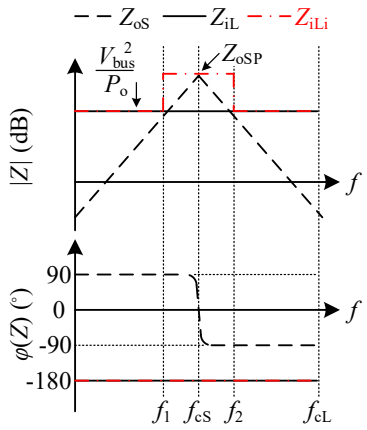


Figure 8. Needs to be modified to: Mechanism of system stability improvement measures.

To maintain the stability of the battery energy storage system, it is essential to isolate the output impedance of the source converter, Z_{os}, from the input impedance of the load converter, Z_{il}. However, this approach may negatively affect the dynamic performance of the load converter. To strike a balance between system stability and the preservation of the dynamic performance of the load converter, the optimal strategy is to adjust Z_{iL} only within the frequency range around the intersection points of $|Z_{oS}|$ and $|Z_{iL}|$, denoted as f_1 and f_2. As illustrated in Figure 8, within the interval $[f_1, f_2]$, altering the magnitude

of Z_{iL} ensures complete separation between Z_{os} and Z_{il}. At this point, the modified input impedance of the load converter, Z_{iLi}, can be expressed as

$$Z_{iLi}(s) = \begin{cases} |Z_{iL1}|e^{j\theta_1} & f \in [f_1, f_2] \\ Z_{iL}(s) & f \notin [f_1, f_2] \end{cases} \tag{17}$$

In this context, Z_{iL} represents the original input impedance of the load converter, while $|Z_{iL1}|$ is the magnitude of the modified impedance within the frequency range $[f_1, f_2]$. The phase associated with $|Z_{iL1}|$ is denoted as θ. To achieve full separation between $|Z_{oS}|$ and $|Z_{iL}|$, the condition $|Z_{iL1}| > |Z_{oSP}|$ must be satisfied. Given that $|Z_{oS}|$ and $|Z_{iL}|$ are completely decoupled within the frequency range $[f_1, f_2]$, the phase θ can take any value. However, in order to minimize disturbances to the load converter's operation, it is advisable to select the phase of the original input impedance of the load converter as θ.

As shown in Figure 9, a virtual impedance Z_{vi} is connected in parallel at the input port of the load converter; the input impedance of the load converter becomes

$$Z'_{iL}(s) = Z_{iL}(s)||Z_{vi}(s) = \frac{Z_{iL}(s) \cdot Z_{vi}(s)}{Z_{iL}(s) + Z_{vi}(s)} \tag{18}$$

where $Z_{iL}(s)$ denotes the original input impedance of the load converter, which is expressed as $-{V_o}^2/P_o$ when the frequency $f < f_{cL}$.

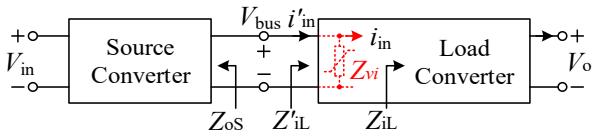


Figure 9. Cascaded system with parallel virtual impedance.

By adjusting $Z_{vi}(s)$, the input impedance of the load converter can be tuned to the ideal impedance, as shown in Figure 7. By substituting (17) into Equation (18), the $Z_{vi}(s)$ required to achieve complete separation of $|Z_{oS}|$ and $|Z_{iL}|$ can be obtained as

$$Z_{vi}(s) = \begin{cases} \frac{-V_{bus}^2|Z_{iL1}|}{V_o^2 - |Z_{iL1}|P_o} & f \in [f_1, f_2] \\ +\infty & f \notin [f_1, f_2] \end{cases} \tag{19}$$

As shown in (19), $Z_{vi}(s)$ remains constant within the range $[f_1, f_2]$, which is defined by the load converter; outside this range, $Z_{vi}(s) = +\infty$. Since f_1 and f_2 are very close to f_{cS}, the source converter also influences the frequency characteristics of $Z_{vi}(s)$. This implies that any changes in the source converter require corresponding adjustments to $Z_{vi}(s)$. However, if $Z_{vi}(s)$ can adaptively respond to variations in the source converter, modifications to the load converter can be avoided. Therefore, the primary goal of the proposed stability control strategy for the battery energy storage system is to enable adaptive impedance reshaping through $Z_{vvjo}(s)$.

3.3. Impedance Remodeling Strategy Based on Input Voltage Feedforward

This study explores strategies to enhance the stability of battery energy storage systems under various operating conditions by optimizing the control of the H-bridge circuit, as shown in Figure 10. To mitigate the impact of dc-link interference on the H-bridge's output voltage, the most straightforward solution is to introduce a signal at point A that counteracts the input voltage disturbance. However, this method is currently complex and lacks flexibility. To overcome these limitations, the disturbance can be shifted to point B

and reshaped using the parallel virtual impedance $Z_{vvjo}(s)$. This modification not only improves system stability but also decouples the input and output voltages.

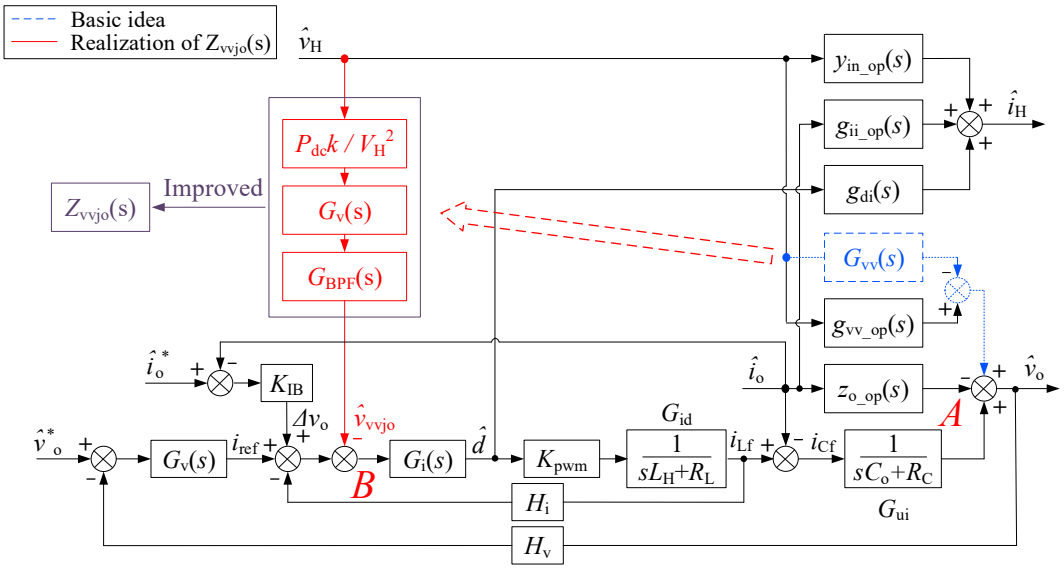


Figure 10. Control strategy of battery energy storage system.

Optimal dynamic performance is typically achieved when the input impedance is tuned to exhibit negative impedance characteristics. However, the presence of $Z_{vvjo}(s)$ can disrupt this behavior, potentially impairing the system's dynamic performance. To mitigate these adverse effects, $Z_{vvjo}(s)$ should be designed to primarily exert influence near the oscillation frequency f_{sc} while having minimal impact across other frequency ranges. As depicted in Figure 11, the design of $Z_{vvjo}(s)$ follows these specific guidelines:

(1) Within the frequency interval $(f_{sc} - \Delta f_{sc}/2, f_{sc} + \Delta f_{sc}/2)$, $Z_{vvjo}(s)$ is configured to behave as positive resistance. The bandwidth Δf_{sc} is defined as $\Delta f_{sc} = f_{sc}/Q_R$, which encompasses the frequencies centered around f_{sc}. Here, Q_R represents the quality factor, with higher Q_R values leading to a narrower effective frequency range for $Z_{vvjo}(s)$. Additionally, k_r is a positive constant that must be determined through further analysis.

(2) Beyond the defined frequency range $(f_{sc} - \Delta f_{sc}/2, f_{sc} + \Delta f_{sc}/2)$, $Z_{vvjo}(s)$ is set to zero, rendering it inactive outside this region.

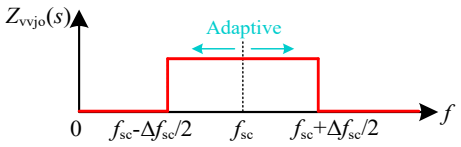


Figure 11. Adaptive characteristics of $Z_{vvjo}(s)$.

From the above analysis and based on Figure 11, the expression for the added virtual impedance $Z_{vvjo}(s)$ can be derived as

$$Z_{vvjo}(s) = \frac{G_{ui}(s)H_v\left[1 + G_{op}(s)\right]}{G_{op}(s)g_{di}(s)Z_{vi}(s)} \tag{20}$$

By substituting (19) into (20), $Z_{vvjo}(s)$ can further be derived as

$$Z_{vvjo}(s) = \begin{cases} \frac{|Z_{iL1}|P_o - V_H^2}{|Z_{iL1}|V_H^2} \cdot \frac{G_{ui}(s)H_v\left[1+G_{op}(s)\right]}{G_{op}(s)g_{di}(s)} & , f \in [f_1, f_2] \\ 0 & , f \notin [f_1, f_2] \end{cases} \tag{21}$$

As indicated in (21), $Z_{vvjo}(s)$ is a frequency-adaptive piecewise function that is active only within the interval $[f_1, f_2]$ and remains zero outside this range. With f_1 and f_2 closely aligned with f_{sc}, $Z_{vvjo}(s)$ can be realized using a bandpass filter $G_{BPF}(s)$ centered at f_{sc}, as described by the following expression:

$$Z_{vvjo}(s) = \frac{|Z_{iL1}|P_o - V_H^2}{|Z_{iL1}|V_H^2} \cdot G_v(s) \cdot G_{BPF}(s) \tag{22}$$

where the expressions for $G_v(s)$ and $G_{BPF}(s)$ are given below:

$$G_v(s) = \frac{G_{ui}(s)H_v\left[1 + G_{op}(s)\right]}{G_{op}(s)g_{di}(s)} \tag{23}$$

$$G_{BPF}(s) = \frac{(2\pi f_{sc}/Q)s}{s^2 + (2\pi f_{sc}/Q)s + (2\pi f_{sc})^2} \tag{24}$$

where Q refers to the quality factor of the bandpass filter, with an initially recommended value of 0.707. As the value of Q increases, the effective frequency range of $Z_{vvjo}(s)$ becomes narrower.

It can be observed that (22) is relatively complex and not easily implementable. Moreover, $Z_{vvjo}(s)$ is influenced by both the circuit parameters and the control configurations. Its precise implementation is further hindered by the tolerances of these parameters and the effects of temperature fluctuations on the circuit components. Additionally, since $Z_{vvjo}(s)$ is linked to the system power, the integration of a power detection circuit is required. This not only increases control complexity but also reduces system reliability. Therefore, to address these challenges, simplifying the virtual impedance control loop becomes essential.

Within the bandwidth governed by $G_{op}(s)$, for frequencies well below the cutoff frequency of $G_{op}(s)$, it is observed that $|G_{op}(s)| >> 1$. Under these conditions, the expression for $G_v(s)$ can be approximated as

$$G_V(s) \approx \frac{G_{ui}(s)H_vG_{op}(s)}{G_{op}(s)g_{di}(s)} = H_v\frac{G_{ui}(s)}{g_{di}(s)} \tag{25}$$

where $G_{ui}(s) = 1/(sC_o + R_c)$; combining (10) with Table 1, the expression of $G_v(s)$ after approximation is as follows:

$$G_v(s) = \frac{H_vV_o^2}{P_{DC}(sC_o + R_C)} \cdot \frac{s^2 + \left(\frac{R_L}{L_H} + \frac{R_C}{L_H}\right)s + \frac{1}{L_HC_o}}{s^2 + \left(\frac{R_L}{L_H} + \frac{R_C}{L_H}\right)s + \frac{1}{L_HC_o} + \frac{V_H^2}{P_{DC}L_H}s} \tag{26}$$

Given that the equivalent series resistances R_L and R_C satisfy $R_L << {V_o}^2/P_o$ and $R_C << {V_o}^2/P_o$, the expression can be further simplified to

$$G_v(s) \approx \frac{H_vV_o^2}{P_{DC}} \cdot \frac{s^2 + \frac{1}{L_HC_o}}{\left(s^2 + \frac{V_H^2}{P_{DC}L_H}s + \frac{1}{L_HC_o}\right)sC_o} \tag{27}$$

From Equation (27), it is observed that G_v behaves like a second-order filter, characterized by a cutoff frequency f_{gv} and a low-frequency gain A_{gv}, which are, respectively, given as

$$f_{gv} = \frac{1}{2\pi\sqrt{L_HC_o}} \approx f_{LC} \tag{28}$$

$$A_{gv} = \frac{H_vV_o^2}{P_{DC}} \tag{29}$$

Since the filter cutoff frequency f_{LC} is much higher than the system oscillation frequency f_{sc}, it can be known through (28) and (29) that the simplified $Z_{vvjo}(s)$ still exhibits a bandpass characteristic centered around f_{sc}. By substituting (28) and (29) into (22), the simplified controller $Z_{vvjo}(s)$ can be obtained as

$$Z_{vvjo}(s) = \frac{D^2 H_v k(2\pi f_{sc}/Q)s}{s^2 + (2\pi f_{sc}/Q)s + (2\pi f_{sc})^2} \tag{30}$$

From (30), it is found that the expression for $Z_{vvjo}(s)$ is simpler and easier to implement, as it is related only to the system oscillation frequency f_{sc}, duty cycle D, constant k, and feedback coefficient H_v. When the system oscillates, the proposed control strategy remains effective regardless of changes in load power.

Based on the above analysis, the digital realization of $Z_{vvjo}(s)$ is illustrated in Figure 12, where the control strategy is transformed into the z-domain. The coefficients of $Z_{vvjo}(s)$ in its difference equation are derived using Equation (30) as follows:

$$\begin{cases} a_1 = -a_2 = b_1 T_s / b_2 \\ a_3 = 2 - b_3 T_s / b_2 \\ a_4 = b_3 T_s / b_2 - b_4 T_s^2 / b_2 - 1 \end{cases} \tag{31}$$

$$\begin{cases} b_1 = \pi D^2 H_v k f_{sc} / Q \\ b_2 = 1 \\ b_3 = 2\pi f_{sc} / Q \\ b_4 = (2\pi f_{sc})^2 \end{cases} \tag{32}$$

where T_s represents the sampling period, set to 40 μs; k is chosen to be 2 to maintain a stable ma.

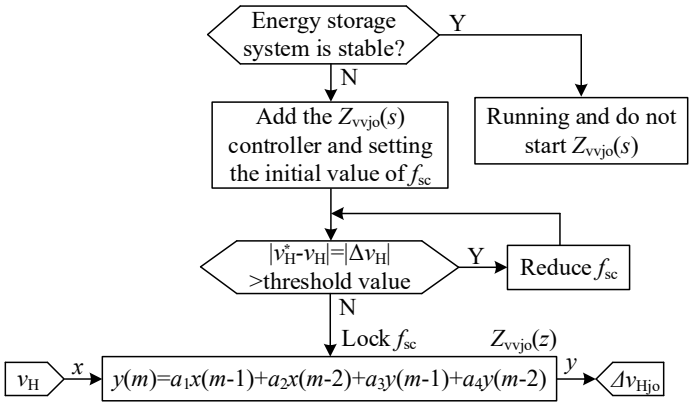


Figure 12. Realization of proposed $Z_{vvjo}(s)$ control strategy.

According to Figure 12, the ac component Δv_H is derived by subtracting the reference voltage v_H^* from the H-bridge input voltage v_H. During stable operation, $|\Delta v_H|$ consists mainly of a small switching ripple. However, when the system becomes unstable, $|\Delta v_H|$ includes a significant low-frequency component at f_{sc}. System stability can thus be assessed by comparing $|\Delta v_H|$ against a threshold, which is set above the maximum permissible ripple and fluctuation of dc voltage during normal operation. If $|\Delta v_H|$ exceeds this threshold, instability is detected, and the $Z_{vvjo}(z)$ control strategy is engaged. $Z_{vvjo}(z)$ control is initially configured using a maximum preset f_{sc}, which can typically be approximated as f_{LC}, given $f_{LC} >> f_{sc}$. If instability persists, it indicates a mismatch between f_{sc} and the actual oscillation frequency. In this case, f_{sc} is gradually reduced until stability is achieved. Once the appropriate f_{sc} value is determined, it remains fixed unless new oscillations

occur. When adjusting f_{sc}, the step size should be much smaller than the bandwidth of the $Z_{vvjo}(z)$ controller to ensure precision. However, overly small steps should be avoided to prevent the locking of f_{sc} at an inaccurate value, which could compromise the system's control effectiveness.

4. Simulation and Experimentation

4.1. Simulation Verification

Based on the above theoretical analysis, a simulation was conducted to verify the proposed impedance reshaping strategy based on input voltage feedforward. A 10 kW simulation model was developed in Simulink, and the circuit structure is shown in Figure 2. The relevant circuit parameters are listed in Table 2. The impedance model of the energy storage converter was established and divided into two different source–load scenarios. It was found that when the dc-link side acts as the source and the converter handles the one-quarter power discharge conditions of the battery, due to the H-bridge output voltage V_o being affected by the LLC input voltage V_{dc}, the amplitude–frequency curves at 650 Hz and 1000 Hz in the Bode plots of the load converter $Z_{S2} + R_B$ and the source converter Z_{S1} intersect. Only at an intersection frequency of 1000 Hz does the phase angle difference exceed 180°, resulting in system instability under this condition. After impedance reshaping through the parallel virtual impedance $Z_{vvjo}(s)$, the Bode plots of the load converter $Z_{S2} + R_B + Z_{vvjo}$ and the source converter Z_{S1}, as well as the Nyquist plot of the impedance ratio $T_m^* = (Z_{S2} + R_B + Z_{vvjo})/Z_{S1}$ are obtained, as shown in Figure 13.

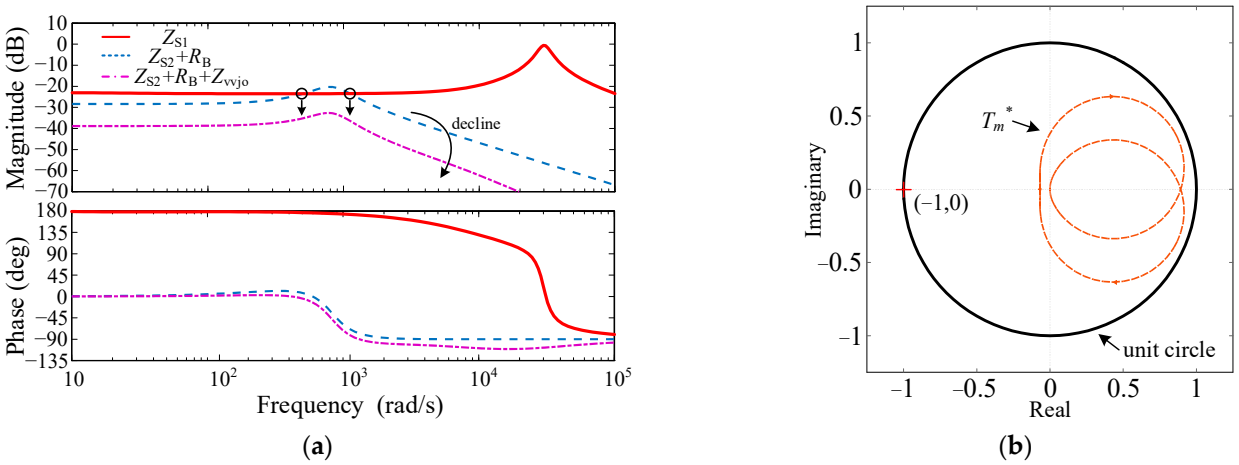


Figure 13. Bode and Nyquist plots after impedance reshaping: (**a**) Bode plots of $Z_{s2} + R_B + Z_{vvjo}$ and Z_{s1}; (**b**) Nyquist plot of T_m*.

Table 2. Simulation and experimental parameters.

Descriptions	Acronym	Values
DC-link voltage	v_{dc}	400 V
Output voltage	v_o	−80 V~80 V
Battery voltage	V_B	340 V~460 V
LLC resonant inductor	L_γ	5.76 µH
LLC resonant capacitor	C_γ	110 nF
LLC switching frequency	f_{LLC}	155 kHz
H-bridge switching frequency	f_H	100 kHz
Input filter capacitor	C_e	600 µF
Output filter capacitor	C_o	22 µF
Output filtering inductance	L_H	40 µH

In Figure 13a, it can be observed that by introducing the parallel virtual impedance $Z_{vvjo}(s)$ into the energy storage converter system, the magnitude of the load converter

Z_{S2} + R_B is reduced by 10 dB. Consequently, the magnitude curves of the source converter Z_{S1} and the impedance-reshaped load converter Z_{S2} + R_B + Z_{vvjo} no longer intersect. Figure 13b shows the Nyquist diagram of the impedance ratio T_m*. When the energy storage converter system employs the parallel virtual impedance $Z_{vvjo}(s)$ for impedance reshaping, the T_m* curve is confined within the unit circle (i.e., $|T_m^*| << 1$) and does not encircle the point (−1, 0). Through an analysis of the Bode plots and Nyquist diagram, it is evident that the strategy of introducing the parallel virtual impedance $Z_{vvjo}(s)$ for impedance reshaping stabilizes the energy storage converter system.

Figure 14 presents the simulated waveforms of the H-bridge input voltage v_{hin} and the output voltage v_o under one-quarter battery discharge power conditions, with the dc-link side serving as the source. As shown in Figure 14, prior to time t_1, the energy storage converter employs dual-loop control in conjunction with a charge–discharge current correction and compensation strategy, resulting in oscillations in both v_{hin} and v_o. The oscillation amplitudes of v_{hin} and v_o reach 8 V and 17 V, respectively, indicating that the battery energy storage system operates in an unstable state. At time t_1, when the parallel virtual impedance $Z_{vvjo}(s)$ is introduced for impedance reshaping, the waveforms of v_{hin} and v_o no longer exhibit oscillations, and the battery energy storage system returns to stable operation.

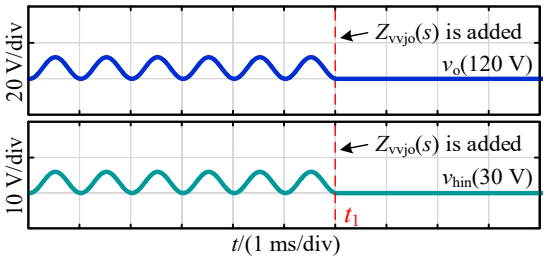


Figure 14. Simulation waveforms before and after adding $Z_{vvjo}(s)$ control.

Figure 15 illustrates the simulation waveforms at a dc-link voltage of 375 V in a battery charging scenario, where the discharge current command is first reduced from 30 A to 15 A and then increased from 15 A back to 30 A. After the parallel virtual impedance $Z_{vvjo}(s)$ is introduced for impedance reshaping, the current command is altered at 0.1 s. As a result, the battery's charge–discharge current promptly converges to the command value within 5 ms, while the battery energy storage system remains in stable operation.

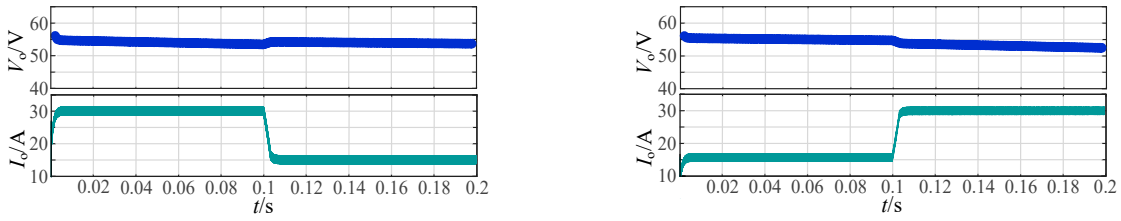


Figure 15. Simulation waveform of battery current change: (**a**) current is reduced from 30 A to 15 A; (**b**) current is increased from 15 A to 30 A.

Figure 16 illustrates the simulation waveforms of the energy storage converter operating at a constant charging current of 30 A. At t = 0.2 s, the dc-link-side voltage undergoes a sudden drop from 375 V to 325 V, followed by a sudden increase from 325 V back to 375 V. From Figure 16, it can be observed that once the parallel virtual impedance $Z_{vvjo}(s)$ is introduced for impedance reshaping, the battery energy storage system remains free of oscillations in response to these abrupt dc-link voltage changes. The converter output

continues to supply a constant charging current, while the output voltage is capable of compensating for the difference between the dc-link voltage and the battery voltage within 10 ms. Consequently, the energy storage converter system achieves effective decoupling between its input and output sides.

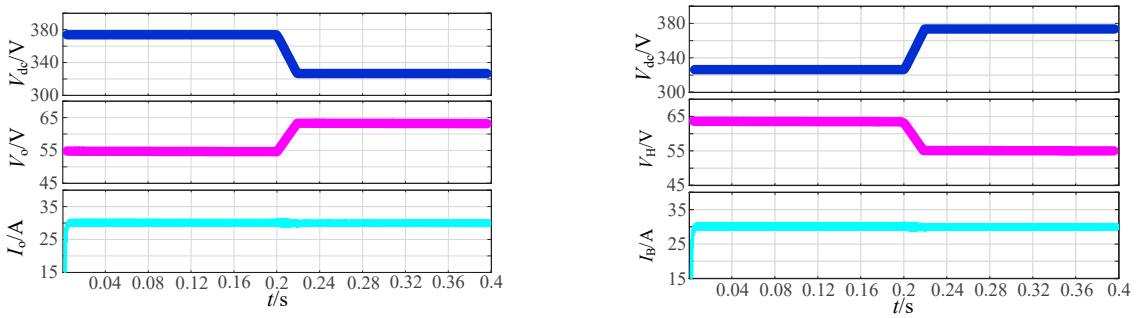


Figure 16. Simulation waveform of dc-link voltage's sudden reduction and sudden increase: (**a**) sudden drop in dc-link voltage; (**b**) sudden increase in dc-link voltage.

4.2. Experimental Verification

To further validate the feasibility of the proposed input-voltage-feedforward-based impedance reshaping strategy, a 10 kW energy storage converter system was constructed as an experimental platform. The parameters of this experimental platform were consistent with those employed in the simulations. A Kewell programmable electronic load was used to emulate the battery, while a Chroma constant-voltage source served as the dc link. The experimental setup is shown in Figure 17.

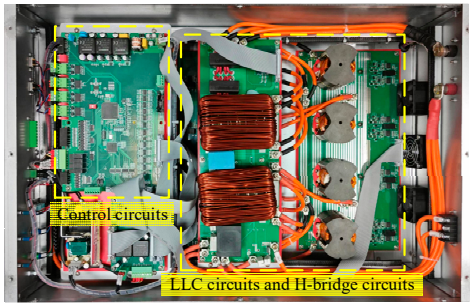


Figure 17. Battery storage converter experimental setup.

Figure 18 presents the experimental waveforms of the energy storage converter system when the dc-link side serves as the source and the converter operates under one-quarter battery discharge conditions. In this setup, the parallel virtual impedance $Z_{vvjo}(s)$ is introduced for impedance reshaping. Prior to the implementation of $Z_{vvjo}(s)$, the LLC resonant converter output voltage (namely, the H-bridge input voltage v_{hin}) exhibits oscillations with an amplitude of 10 V, while the H-bridge output voltage v_o oscillates with an amplitude of 6 V. After the introduction of $Z_{vvjo}(s)$ for impedance reshaping, both v_{hin} and v_o no longer oscillate, and the energy storage converter system reaches a stable operating state.

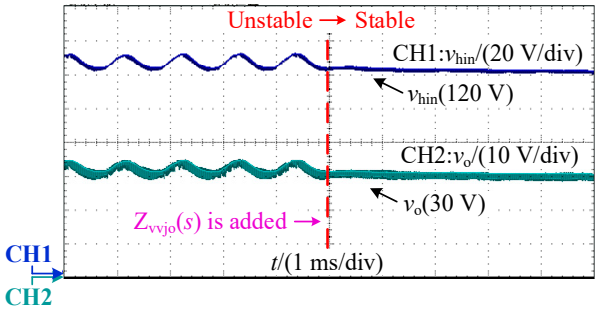


Figure 18. Dynamic switching process.

Figure 19 illustrates the experimental waveforms under battery discharge conditions with the dc-link side serving as the power source, focusing on transient changes in the current command. As shown in Figure 19a, before the virtual impedance $Z_{vvjo}(s)$ is introduced, the battery discharge current transitions from 10 A to 30 A in 6 ms and from 30 A to 14 A in 5 ms. According to Figure 19b, after the system exhibits oscillations, incorporating $Z_{vvjo}(s)$ in the control loop for impedance reshaping eliminates these oscillations under output current disturbances. Following impedance reshaping, the battery discharge current transitions from 10 A to 30 A in 12 ms and from 30 A to 10 A in 8 ms. A comparative analysis reveals a maximum delay of 6 ms in the dynamic response, confirming that the parallel virtual impedance $Z_{vvjo}(s)$ effectively stabilizes the energy storage converter system without excessively compromising the dynamic performance of the control loop.

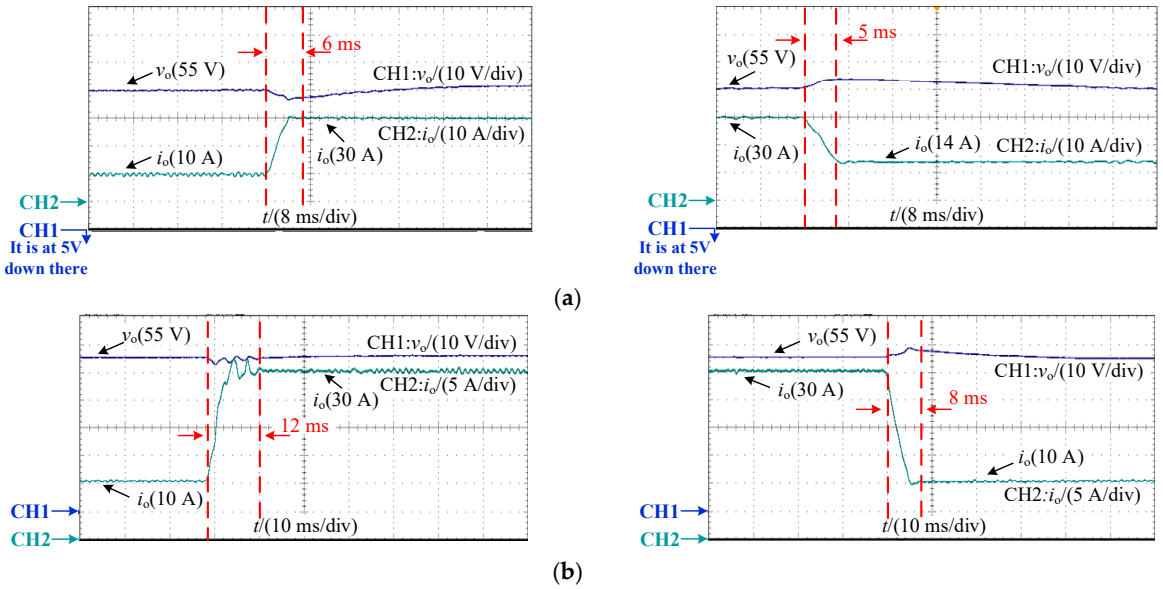


Figure 19. Experimental waveform of battery current change: (**a**) virtual impedance $Z_{vvjo}(s)$ not added; (**b**) virtual impedance $Z_{vvjo}(s)$ added.

Figure 20 presents the experimental waveforms under battery discharge conditions with the dc-link side serving as the source, where the battery energy storage converter incorporates the parallel virtual impedance $Z_{vvjo}(s)$. In this test, the dc-link voltage experiences abrupt drops and rises. As shown in Figure 20, following these sudden dc-link voltage disturbances, both the input voltage v_{dc} and the output voltage v_o of the battery energy storage converter stabilize within 20 ms, indicating strong disturbance rejection. The experimental waveform trends are consistent with the simulation results. These findings confirm that the proposed strategy of introducing $Z_{vvjo}(s)$ into the energy storage converter for impedance reshaping effectively ensures the stable operation of the battery

energy storage system, achieves decoupling between the input and output sides, and meets practical application requirements.

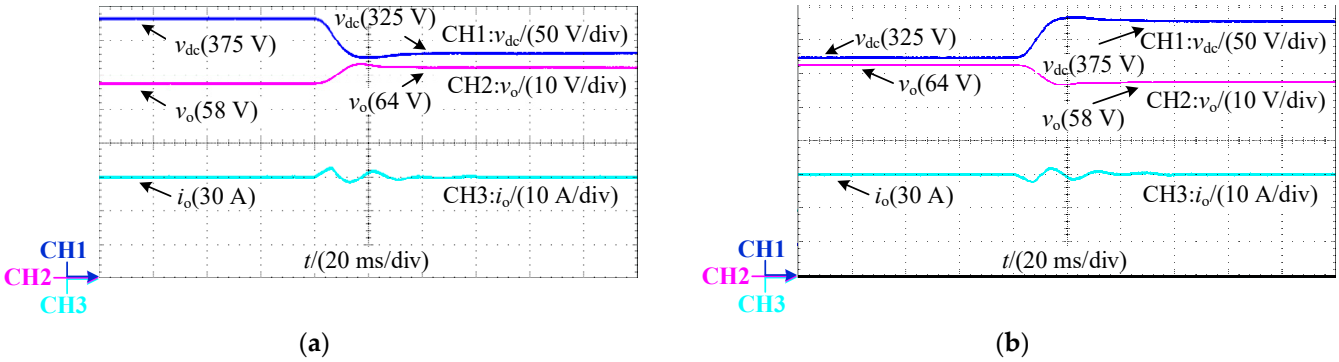


Figure 20. Experimental waveforms for dc-link variation: (**a**) sudden drop in dc-link voltage; (**b**) sudden increase in dc-link voltage.

5. Conclusions

This study focuses on the examination of S-PPC-type battery energy storage systems. Through full consideration of the mutual coupling effects between the converter and the dc-link side and the battery-series end and the interactions between the front and rear stages, impedance modeling was conducted to obtain more accurate modeling results, thereby compensating for the mismatch between the impedance model and the actual system. Based on the established model, the impedance ratio criterion was used to analyze the stability of the energy storage converter system under different operating conditions. At the same time, stability improvement measures for the energy storage system were proposed. Through the incorporation of the virtual impedance $Z_{vvjo}(s)$, the converter's input impedance was selectively modified in a narrow band around the system's oscillation frequency. The addition of the virtual impedance $Z_{vvjo}(s)$ enhanced the stability of the battery energy storage system, while the proposed solution is easy to implement and possesses high reliability.

In addition to the demonstrated improvements in stability and energy efficiency, the CG S-PPC battery energy storage converter offers significant economic and environmental benefits. The reduction in converter size and power handling requirements lowers costs, while the energy savings achieved through partial power processing contribute to environmental sustainability. These factors enhance the practicality and appeal of S-PPC technology for large-scale battery energy storage systems, paving the way for broader adoption in applications that demand cost-effectiveness, high efficiency, and compliance with sustainability goals.

Author Contributions: Conceptualization, M.L. and Y.W.; methodology, Y.W. and X.X.; software, Y.W. and B.X.; validation, X.X., Y.W. and B.X.; formal analysis, M.L., Y.W. and X.X.; investigation, H.L. and L.J.; writing—original draft preparation, Y.W.; writing—review and editing, Y.W.; visualization, M.L.; supervision, L.J.; funding acquisition, M.L. All authors have read and agreed to the published version of the manuscript.

Funding: This research was funded by the Technology Plan Project of Liaoning Province of China, under grant number 2021J116/10500221.

Data Availability Statement: The data presented in this study are available on request from the corresponding author. The data are not publicly available due to private reasons.

Conflicts of Interest: Authors Ming Li, Yucheng Wu, Xiangxin Xi and Haibo Liu were employed by Aerospace Changfeng Chaoyang Power Co., Ltd., Beijing Aerospace Changfeng Co., Ltd. Author Baizheng Xu was employed by Dongying Power Supply Company, State Grid Shandong Electric Power Company. The remaining author declares that the research was conducted in the absence of any commercial or financial relationships that could be construed as a potential conflict of interest.

References

1. Nazaralizadeh, S.; Banerjee, P.; Srivastava, A.K.; Famouri, P. Battery Energy Storage Systems: A Review of Energy Management. *Syst. Health Metr.* **2024**, *17*, 1250.
2. Stanko, P.; Tkac, M.; Kajanova, M.; Roch, M. Impacts of Electric Vehicle Charging Station with Photovoltaic System and Battery Energy Storage System on Power Quality in Microgrid. *Energies* **2024**, *17*, 371. [CrossRef]
3. Li, J.; Fang, Z.; Wang, Q.; Zhang, M.; Li, Y.; Zhang, W. Optimal Operation with Dynamic Partitioning Strategy for Centralized Shared Energy Storage Station with Integration of Large-scale Renewable Energy. *J. Mod. Power Syst. Clean Energy* **2024**, *12*, 359–370. [CrossRef]
4. Naguib, M.; Kollmeyer, P.; Emadi, A. Lithium-Ion Battery Pack Robust State of Charge Estimation, Cell Inconsistency, and Balancing: Review. *IEEE Access* **2021**, *9*, 50570–50582. [CrossRef]
5. Li, X.; Lyu, L.; Geng, G.; Jiang, Q.; Zhao, Y.; Ma, F.; Jin, M. Power Allocation Strategy for Battery Energy Storage System Based on Cluster Switching. *IEEE Trans. Ind. Electron.* **2022**, *69*, 3700–3710. [CrossRef]
6. Song, J.; Zhang, W.; Liang, H.; Jiang, J.; Yu, W. Fault-Tolerant Control for a Flexible Group Battery Energy Storage System Based on Cascaded Multilevel Converters. *Energies* **2018**, *11*, 171. [CrossRef]
7. Ghaeminezhad, N.; Ouyang, Q.; Hu, X.; Xu, G.; Wang, Z. Active Cell Equalization Topologies Analysis for Battery Packs: A Systematic Review. *IEEE Trans. Power Electron.* **2021**, *36*, 9119–9135. [CrossRef]
8. Lujun, W.; Jinyang, K.; Min, Z.; Aina, T.; Tiezhou, W.; Xiaoxing, Z.; Jiuchun, J. Efficient and Fast Active Equalization Method for Retired Battery Pack Using Wide Voltage Range Bidirectional Converter and DBSCAN Clustering Algorithm. *IEEE Trans. Power Electron.* **2022**, *37*, 13824–13833. [CrossRef]
9. Zhang, R.; Wang, S.; Cao, Z.; Chung, H.S.H. A Galvanic-Isolated Automatic Equalization Charging System for Series-Connected Cells or Battery Strings. *IEEE Trans. Ind. Electron.* **2024**, *71*, 13943–13954. [CrossRef]
10. Cao, Y.; Ngo, M.; Yan, N.; Dong, D.; Burgos, R.; Ismail, A. Design and Implementation of an 18-kW 500-kHz 98.8% Efficiency High-Density Battery Charger with Partial Power Processing. *IEEE J. Emerg. Sel. Top. Power Electron.* **2022**, *10*, 7963–7975. [CrossRef]
11. Ye, D.; Martinez, S. A Three-Port DC-DC Converter with Partial Power Regulation for a Photovoltaic Generator Integrated with Energy Storage. *Electronics* **2024**, *13*, 2304. [CrossRef]
12. Santos, N.G.F.d.; Zientarski, J.R.R.; Martins, M.L.d.S. A Review of Series-Connected Partial Power Converters for DC–DC Applications. *IEEE J. Emerg. Sel. Top. Power Electron.* **2022**, *10*, 7825–7838. [CrossRef]
13. Anzola, J.; Aizpuru, I.; Arruti, A. Non-Isolated Partial Power Converter for Electric Vehicle Fast Charging Stations. In Proceedings of the 2020 IEEE 11th International Symposium on Power Electronics for Distributed Generation Systems (PEDG), Dubrovnik, Croatia, 28 September–1 October 2020; pp. 18–22.
14. Tian, Y.; Li, Y.; Cao, B.; Wei, F.; Zheng, Y. Systematic Topology Synthesis and Power Density Visualization of Partial Power Processing Architecture. *IEEE Trans. Power Electron.* **2025**, *40*, 1346–1358. [CrossRef]
15. Anzola, J.; Aizpuru, I.; Romero, A.A.; Loiti, A.A.; Lopez-Erauskin, R.; Artal-Sevil, J.S.; Bernal, C. Review of Architectures Based on Partial Power Processing for DC-DC Applications. *IEEE Access* **2020**, *8*, 103405–103418. [CrossRef]
16. Gsous, O.; Rizk, R.; Barbón, A.; Georgious, R. Review of DC-DC Partial Power Converter Configurations and Topologies. *Energies* **2024**, *17*, 1496. [CrossRef]
17. Xue, F.; Yu, R.; Huang, A. A Family of Ultrahigh Efficiency Fractional dc–dc Topologies for High Power Energy Storage Device. *IEEE J. Emerg. Sel. Top. Power Electron.* **2021**, *9*, 1420–1427. [CrossRef]
18. Sang, X.; Gao, S.; Wang, Y.; Xu, D. A High Step-up Partial Power Regulated DC–DC Converter with Zero Input Current Ripple and Wide Input Range. *IEEE Trans. Ind. Electron.* **2024**, *71*, 14097–14110. [CrossRef]
19. Mira, M.C.; Zhang, Z.; Jørgensen, K.L.; Andersen, M.A.E. Fractional Charging Converter with High Efficiency and Low Cost for Electrochemical Energy Storage Devices. *IEEE Trans. Ind. Appl.* **2019**, *55*, 7461–7470. [CrossRef]
20. Hou, N.; Ding, L.; Gunawardena, P.; Wang, T.; Zhang, Y.; Li, Y.W. A Partial Power Processing Structure Embedding Renewable Energy Source and Energy Storage Element for Islanded DC Microgrid. *IEEE Trans. Power Electron.* **2023**, *38*, 4027–4039. [CrossRef]
21. Tang, C.Y.; Wang, C.W.; Chien, H.C. A Dynamic Smooth Transition Control Integrated with Hybrid Modulation for Wide Output Voltage Range Bidirectional CLLC Resonant Converters. *IEEE Trans. Power Electron.* **2023**, *38*, 13587–13593. [CrossRef]

22. Zheng, K.; Zhang, W.; Wu, X.; Jing, L.; Zhao, H. Partial-Power Conversion for Increased Energy Storage Capability of Li-Ion Battery Energy Storage System. *IEEE Trans. Ind. Electron.* **2024**, *71*, 4742–4752. [CrossRef]
23. Cheng, C.C.; Gao, J.T.; Lo, K.Y. Hot-Swappable Grid-Connected Multilevel Converter for Battery Energy Storage System. *IEEE Trans. Circuits Syst. II Express Briefs* **2020**, *67*, 2109–2113. [CrossRef]
24. Nabinejad, A.; Rajaei, A.; Mardaneh, M. A Systematic Approach to Extract State-Space Averaged Equations and Small-Signal Model of Partial-Power Converters. *IEEE J. Emerg. Sel. Top. Power Electron.* **2020**, *8*, 2475–2483. [CrossRef]
25. Agamy, M.S.; Harfman-Todorovic, M.; Elasser, A.; Chi, S.; Steigerwald, R.L.; Sabate, J.A.; McCann, A.J.; Zhang, L.; Mueller, F.J. An Efficient Partial Power Processing DC/DC Converter for Distributed PV Architectures. *IEEE Trans. Power Electron.* **2014**, *29*, 674–686. [CrossRef]
26. Kwon, Y.D.; Freijedo, F.D.; Wijekoon, T.; Liserre, M. Series Resonant Converter-Based Full-Bridge DC–DC Partial Power Converter for Solar PV. *IEEE J. Emerg. Sel. Top. Power Electron.* **2024**, *12*, 1719–1729. [CrossRef]
27. Gu, R.; Duan, J.; Zhang, D.; Liu, H. Regulated Series Hybrid Converter With DC Transformer (DCX) for Step-Up Power Conversion. *IEEE Trans. Ind. Electron.* **2022**, *69*, 8961–8971. [CrossRef]
28. Zhang, X.; Ruan, X.; Zhong, Q.C. Improving the Stability of Cascaded DC/DC Converter Systems via Shaping the Input Impedance of the Load Converter with a Parallel or Series Virtual Impedance. *IEEE Trans. Ind. Electron.* **2015**, *62*, 7499–7512. [CrossRef]
29. Cespedes, M.; Xing, L.; Sun, J. Constant-Power Load System Stabilization by Passive Damping. *IEEE Trans. Power Electron.* **2011**, *26*, 1832–1836. [CrossRef]
30. Rahimi, A.M.; Emadi, A. Active Damping in DC/DC Power Electronic Converters: A Novel Method to Overcome the Problems of Constant Power Loads. *IEEE Trans. Ind. Electron.* **2009**, *56*, 1428–1439. [CrossRef]
31. Cai, W.; Yi, F.; Cosoroaba, E.; Fahimi, B. Stability Optimization Method Based on Virtual Resistor and Nonunity Voltage Feedback Loop for Cascaded DC–DC Converters. *IEEE Trans. Ind. Appl.* **2015**, *51*, 4575–4583. [CrossRef]
32. Liu, B.; Ben, H.; Zhang, X.; Meng, T.; Wang, X. Stabilization of a Cascaded AC–DC–DC System with Small Bus Capacitance Based on Small Signal Analysis. *IEEE Trans. Ind. Appl.* **2018**, *54*, 4650–4659. [CrossRef]
33. Purgat, P.; Shah, S.; Qin, Z.; Bauer, P. Design criteria of solid-state circuit breaker for low-voltage microgrids. *IET Power Electron.* **2021**, *14*, 1284–1299. [CrossRef]
34. Liu, F.; Ruan, X.; Huang, X.; Qiu, Y. Second Harmonic Current Reduction for Two-Stage Inverter With DCX-LLC Resonant Converter in Front-End DC–DC Converter: Modeling and Control. *IEEE Trans. Power Electron.* **2021**, *36*, 4597–4609. [CrossRef]

Disclaimer/Publisher's Note: The statements, opinions and data contained in all publications are solely those of the individual author(s) and contributor(s) and not of MDPI and/or the editor(s). MDPI and/or the editor(s) disclaim responsibility for any injury to people or property resulting from any ideas, methods, instructions or products referred to in the content.